ARTICLE

Check for updates

Realization of photonic charge-2 Dirac point by engineering super-modes in topological superlattices

Mengying Hu[1,3], Kun Ding [2,3], Tong Qiao[1], Xi Jiang[1], Qiang Wang[1], Shining Zhu[1] & Hui Liu [1✉]

Quite recently, an unconventional variety of fourfold linear band degeneracy points has been discovered in certain condensed-matter systems. Contrary to standard 3-D Dirac monopoles, these quadruple points known as the charge-2 Dirac points are characterized by nonzero topological charges, which can be exploited to delve into hitherto unknown realms of topological physics. Here, we report on the experimental realization of a charge-2 Dirac point by deliberately engineering hybrid topological states, called super-modes, in a 1-D optical superlattice system with synthetic dimensions. Utilizing direct reflection and transmission measurements, we propose the existence of the synthetic charge-2 Dirac point in the visible region. We also show an experimental approach to manipulating two spawned Weyl points possessing equal charge. Topological end modes resulting from the charge-2 Dirac point can be delicately controlled within truncated superlattices, opening a pathway to rationally engineer local fields with intense enhancement.

[1] National Laboratory of Solid State Microstructures, School of Physics, Collaborative Innovation Center of Advanced Microstructures, Nanjing University, 210093 Nanjing, China. [2] The Blackett Laboratory, Department of Physics, Imperial College London, London SW7 2AZ, UK. [3] These authors contributed equally: Mengying Hu, Kun Ding. ✉email: liuhui@nju.edu.cn

Ever since the remarkable discovery that fermion-like energy excitations predicted by relativistic quantum field theories can emerge in electronic crystals whose band structures display linear band degeneracy points, a great deal of theoretical and experimental interest has been attracted in exploring such materials known as topological semimetals. The corresponding gapless semimetal phases are regarded as novel topological states, which open a new era in investigating condensed-matter physics. Substantial attention is engaged by Weyl points (WPs)[1–6] and 3-D Dirac points (DPs)[7,8]. WPs that reported actively in electronic systems are identified as synthetic magnetic monopoles in momentum space, carrying topological charges (Chern numbers) of ±1 and featured by "Fermi arc" surface states[6,9]. DPs can be viewed as two overlapping WPs with opposite topological charges, predicted and observed in crystals as well. However, it has been recently demonstrated that unconventional topological points appear in certain crystal structures[10–18], which cannot be described in accordance with an emergent relativistic field theory. On such candidate is the charge-2 Dirac point (CDP), existing as a double-Weyl phonon in transition metal monosilicides[14,15]. It's generated by merging a pair of identically charged WPs, and hence possessing the topological charge of ±2. Consequently, CDPs are radically distinct from traditional DPs and can give rise to novel physical phenomena.

While topological semimetals found in nature exhibit exotic phases of matter, great process in understanding such band topology has also been impelled by the research on engineered systems. The core idea of engineering lattices is to create emergent band structures analogous to those formed in electronic crystals, which can be highly tunable and have fundamentally discriminative properties, providing us unprecedented opportunities of studying topological physics. Recent developments of experimental techniques have propelled ultracold atomic gases[19,20], photonics[4,21–26], and acoustics[27–30] as promising systems to engineer WPs and DPs with novel emergent properties. Constructing complex 3-D structures with certain symmetry broken is perceived as the most common strategy[4,21–24,27–29], whereas another route to realize topological points is based on synthetic dimensions[30–35]. The initial motivation for employing synthetic dimensions was to explore fundamental physical effects in a space with a higher dimensionality via introducing controllable artificial dimension(s) in addition to the real spatial degree(s), in especial topological effects within systems beyond 3-D space. However, lately the interest of synthetic dimensions is fueled by the capacity to study topological features of 3-D degenerate points in 2-D (1-D) systems, dramatically simplifying experimental designs[19,26,30,34,36,37]. Either of the methods has been extensively exploited for WPs and DPs in the recent years. Nevertheless, as for the CDP, the only engineered system supporting it reported so far is made up of an acoustic metamaterial corresponding to a classical 3-D phononic crystal with a nonsymmorphic structure[38]. To our knowledge, in the visible regime, neither 3-D engineered systems nor 2-D (1-D) structures equipped with synthetic dimensions have been established to realize CDPs.

Here, we propose an experimentally feasible scheme to realize CDPs in a 1-D optical superlattice system with working frequencies lying in the visible region harnessing synthetic dimensions, and manipulate the spawned WPs with the same topological charges. To attain this, we start by designing suitable photonic modes interacting with each other to form a 1-D superlattice. Instructively, interfaces between distinct topological phases of matter host robust and exotic quantum states, the use of which acts as a strong driver of current research in condensed matter[39–43]. Hence, we stack together two kinds of photonic crystals (PCs) belonging to different class of topology to create

such topological interface modes (TIMs), and on this basis topological states of photons associated with CDPs can be fully investigated under the introduction of synthetic space, facilitating the experimental realization, which is otherwise elusive at such frequencies. Furthermore, intriguing topological-protected end modes emerge at the termini of the truncated superlattice, guaranteed by the CDP with nonzero topological charge. More precisely, these end modes uniquely result from the bulk-edge correspondence[44] for each of the two WPs producing the CDP in synthetic space, which in turn could be tuned independently. Such topological end modes resemble surface states in Weyl semimetals[2,3,6], holding great potential for applications in non-linear optics[45], quantum optics[46], and lasers[47] owing to strongly enhanced localized fields.

Results

Design concept of the creation of CDPs. The starting point of our scheme is to construct a 1-D topological superlattice by use of TIMs existing at interface of two PCs with discriminative topological class. Specifically, our lattice consists of these two PCs stacked alternatively, in which each interface supports a TIM that hybridizes with each other to form a novel variety of artificial collective modes, resulting in a 1-D superlattice band structure where a single TIM serves as the photonic orbital. Similar heterostructures have previously been rendered for grapheme nanoribbons[41,42] and topological insulator superlattices[43].

For CDPs to occur, we require two more dimensions added to the wave vector dimension provided by the existing 1-D superlattice. It's noticeable that the coupling of nearest-neighbor TIMs, inclusive of both the magnitude and the sign, can be feasibly tuned by altering the repeated number of the PC's unit cell between adjacent interfaces. Moreover, the on-site resonance frequency of a TIM can be highly controllable if we put a defective unit with adjustable thickness at the interface. Therefore, the modulation of the coupling between adjacent TIMs and the on-site frequency of a single TIM is readily available, which allows us to parameterize these two variables and treats them as two artificial momentum dimensions. Through meticulous design, WPs can thus arise in such 3-D synthetic space owing to the hybrid modes designated as the super-modes, but the realization of CDPs begs for the overlap of two equivalently charged WPs. To this end, we exploit the polarization degree of light. The fact that TIMs response discriminately to transverse-magnetic (TM) and transverse-electric (TE) polarized light appends a so-called 'pseudospin' degree of freedom to the synthetic space, and the appearance of a CDP is finally achieved by merging a pair of WPs with the same topological charge but different pseudospins. Surprisingly, the CDP can conversely be split into two spawned WPs in synthetic space, whose trajectories are tunable via utilizing the pseudospin degree. Such procedure has never been revealed in practice prior to us, offering the evidence that our proposed artificial systems are used to not only explore topological excitations discovered before, but also navigate a way of studying novel phenomena. In particular, we design an applicable and smart strategy to detect the CDP and spawned WPs straightforwardly, which has never been reported before us.

The adjustability of a single TIM. We first provide a detailed introduction to the proposed structure holding a single TIM that is highly adjustable. As shown in Fig. 1a, it consists of two kinds of PCs (PC-p and PC-q), and a defective unit D. The unit cells of PC-p, PC-q, and the defective unit D are represented as $p = M1_{d1/2}M2_{d2}M1_{d1/2}$, $q = M2_{d2/2}M1_{d1}M2_{d2/2}$, and $D = M1_{d}M2_{d}$. Here, M1 and M2 denote two dielectric materials and the
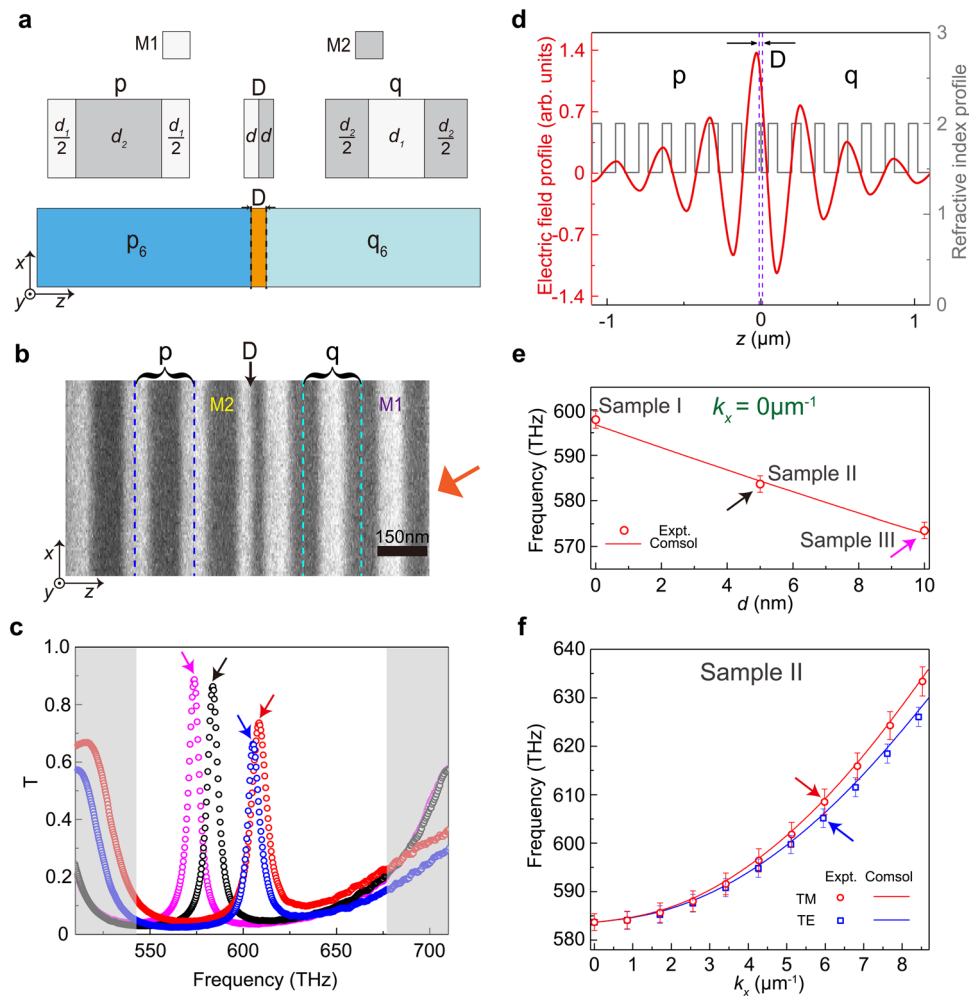
Fig. 1 Construction of one topological interface mode (TIM) and its tunability. a The proposed structure for a single TIM. The upper panel shows the unit cell of both photonic crystals (p-type and q-type unit cell) and the configuration of the defective unit. All of them are made up of alternating layers of two dielectric materials, denoted as M1 (white) and M2 (gray). The thickness notations are indicated on each layer. **b** Scanning electron microscope (SEM) picture of Sample II. The orange arrowhead shows the direction of incident light. Here, we employ HfO_2 as M1 (bright region) and SiO_2 as M2 (dark region). The refractive indices of HfO_2 and SiO_2 are 2 and 1.46, respectively. **c** Measured transmission spectra of Sample II under normal incidence, oblique incidence of transverse-magnetic (TM) waves, and oblique incidence of transverse-electric (TE) waves are shown by black, red, and blue circles, respectively. The oblique incident angle is 30°. The magenta circles show measured transmission spectrum of Sample III under normal incidence. **d** The calculated electric field profile of the TIM for Sample II under normal incidence is plotted by the solid red line. The gray line shows the corresponding refractive index profile. **e** d-dependent resonance frequency of the TIM with $k_x = 0\ \mu m^{-1}$. **f** The in-plane dispersion relation of the TIM for the TM (red line) and TE (blue line) polarizations excited in sample II. In both **e** and **f**, solid lines are calculated by the simulation software COMSOL, and open markers are obtained directly from experimental data. The corresponding experimental transmission spectra of the black, red, blue, and magenta arrowheads in **e** and **f** are shown in **c**. The ranges of ±standard deviation of measured data are shown by the error bars.

subscripts stand for the thickness of associated layers. The stacking structure built up of repeated p(q)-type unit cells can thus be described as $p_6(q_6)$, in which the subscripts are employed to show the number of unit cells. Hence, we adopt p_6Dq_6 to label the structure shown in the bottom of Fig. 1a, which can support a single TIM[48] as discussed in the Supplementary Note 1. Experimentally, such structure is fabricated with e-beam evaporation and we fabricate three samples with identical $d_1 = 70$ nm and $d_2 = 79$ nm, but setting $d = 0$ nm (sample I), $d = 5$ nm (sample II), and $d = 10$nm (sample III), respectively. Figure 1b exhibits the scanning electron microscope (SEM) picture of sample II with the highlighted p-type and q-type unit cells. The measured trans-m0ission spectra of the sample II (III) are given in Fig. 1c by black (magenta) circles under normal incident light ($k_x = 0\ \mu m^{-1}$), where the common band gaps (bands) of the two PCs are highlighted as the white (gray) regions. It can be seen that sharp peaks

inside the gap appear, which are attributed to the excitation of a TIM. To verify this, Fig. 1d exhibits the calculated spatial distribution of the electric field profile for the associated state of Sample II, from which we can see that such state decays rapidly away from the position of D—a distinctive signature of the TIM. We can also see that the TIM peak of sample III lies at the lower frequency than that of sample II in Fig. 1c, showing the d-dependent feature of resonance frequency of TIMs. To make it clear, resonance frequencies of TIMs for these three samples are marked by red open circles in Fig. 1e, decreasing significantly with increasing value of d. This confirms the fact that modulating thickness of the defective unit provides us a feasible strategy to adjust on-site frequencies of TIMs.

Furthermore, the TIM exists for both TM and TE polarizations, but they are degenerate in the case of normal incidence ($k_x = 0\ \mu m^{-1}$). To lift such degeneracy, we need to use oblique
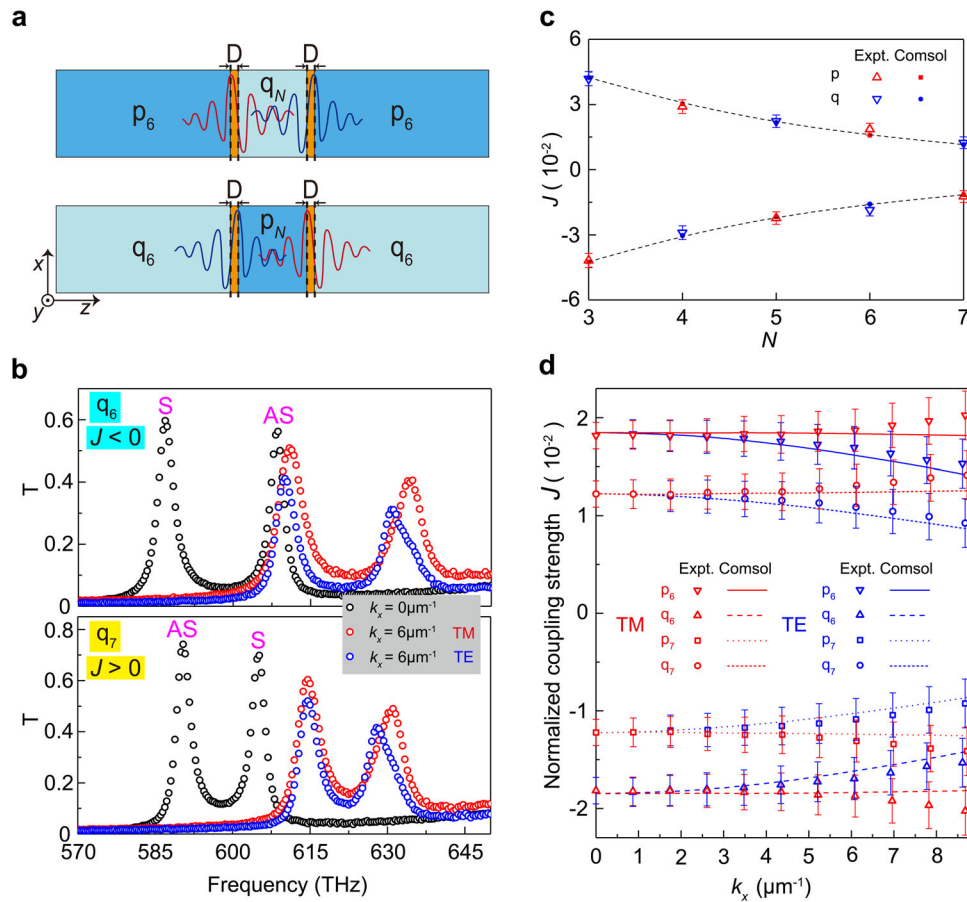
Fig. 2 Coupling signs and magnitudes between two topological interface modes (TIMs). a Sketches of two different designs of coupled TIMs. The red and blue curves show schematic mode profiles of two individual TIMs. **b** Measured transmission spectra of $p_6Dq_6Dp_6$ (upper panel) and $p_6Dq_7Dp_6$ (lower panel) with $k_x = 0\,\mu m^{-1}$ and $k_x = 6\,\mu m^{-1}$ (incident angle 30°) for transverse-magnetic/transverse-electric (TM/TE) polarizations. **c** Normalized coupling strength J as a function of N for both p-type (red markers) and q-type (blue markers) PCs. The filled squares (p-type) and circles (q-type) are calculated by the simulation software COMSOL, whereas open upward-pointing (p-type) and downward-pointing (q-type) triangles are extracted from experimental data. The downward tendency of the magnitude of normalized coupling strength $|J|$ versus the number of unit cells of coupling element N is shown by dotted lines. **d** Dependence of the normalized coupling strength J on the in-plane wave vector k_x for both TM and TE polarizations. All lines are calculated by COMSOL, while open markers are obtained from experimental data. Also shown are the ranges of ±standard deviation for experimental data in **c** and **d** by error bars.

incident light with $k_x \neq 0\,\mu m^{-1}$, and hence we measure the transmission spectra of sample II under the TM (TE) polarized light with oblique incident angles ($k_x = 6\,\mu m^{-1}$), as shown by red (TM) and blue (TE) open circles in Fig. 1c, confirming the removal of the degeneracy. Figure 1f shows the measured TIM frequencies as a function of k_x for Sample II for both polarizations. It is noticeable that the splitting between TM (red) and TE (blue) polarized TIMs increases monotonically with the increment of k_x, matching well with the calculated results (solid lines). Therefore, such splitting between TM and TE polarized TIMs affords us another degree of freedom to manipulate the TIMs.

Coupling signs and magnitudes between two TIMs. Next, we investigate the effects of q-type and p-type PCs as the coupling channel between two TIMs. As shown schematically in Fig. 2a, each structure is made up of stacking PCs (p-type and q-type) separated by two defective units. With the same notation in Fig. 1a, two designs in Fig. 2a can then be denoted as $p_6Dq_ND p_6$ and $q_6Dp_ND q_6$, respectively, where the subscript N is the number of unit cells of associated PC. The overlapping of two individual TIMs with the same frequency ω_0 gives rise to two hybridized TIMs, one symmetric mode (S) at ω_S and one antisymmetric one

(AS) at ω_{AS}. Here, the symmetric types are defined by the symmetry of the electric field which uses the center of $p_N(q_N)$ as the reference point. In the following, we demonstrate that the normalized coupling strength $J \equiv (\omega_S - \omega_{AS})/2\omega_0$ (see Methods), which describes the coupling amplitudes and signs, is directly controlled by N for either q-type or p-type PC in the middle.

We start by considering the q-type PC as the coupling elements, namely $p_6Dq_ND p_6$ with normal incidence ($k_x = 0\,\mu m^{-1}$). Figure 2b shows the transmission spectra of $p_6Dq_6D p_6$ and $p_6Dq_7Dp_6$ (black circles). The parameters of both p-type and q-type unit cells are identical to those in Fig. 1b except that d of the defective unit is 0 nm. For both samples, we see two transmission peaks owing to two hybridized TIMs (S and AS). For the sample $p_6Dq_6D p_6$, $\omega_S < \omega_{AS}$ such that $J < 0$. While for the sample $p_6Dq_7Dp_6$, $\omega_S > \omega_{AS}$ such that $J > 0$. In Fig. 2c, the N-dependence of J for q-type PC case, which is extracted from experimental data, is shown by blue downward-pointing triangles. We can see that $|J|$ possesses a negative association with N, and the sign of J totally relies on the parity of N. For the samples $p_6Dq_ND p_6$, if N is odd, $J < 0$, otherwise $J > 0$. This is because the accumulated phase for each unit cell is π.

We then explore J for the p-type PC as the coupling channel case, namely the samples $q_6Dp_ND q_6$. The corresponding results are present as red upward-pointing triangles in Fig. 2c, in which J

has the same magnitude as that of $p_6Dq_NDp_6$ but with opposite signs for a given N. In order to confirm these results, we also plot the results calculated by a commercial finite element simulation software (COMSOL) in Fig. 2c, which shows good agreements with experimental ones. The sign of J is determined by the coupling between two TIMs. More details of two coupled TIMs are provided in the in the Supplementary Note 2.

Moreover, we investigate coupling effects for nonzero in-plane wave vector ($k_x < 0\,\mu m^{-1}$). Figure 2b also depicts the measured transmission spectra of the two samples $p_6Dq_6Dp_6$ and $p_6Dq_7Dp_6$ for TM (red open circles) and TE (blue open circles) polarizations with $k_x = 6\,\mu m^{-1}$, indicating the polarization-dependent characteristic of the hybridized TIMs. To get a further step, we plot J as a function of k_x in Fig. 2d, where $p_6(q_6)$ and $p_7(q_7)$ are employed as representatives of the even and odd N cases. The result clearly shows that the sign of J changes in the same way as that of $k_x = 0\,\mu m^{-1}$. However, given a fixed $p_N(q_N)$, the magnitude of J due to the TM mode has discriminated variation tendency compared with J of the TE one as k_x increases, which almost remains the same for the former while decreases significantly for the latter. The calculated results achieved by a COMSOL via the optic module are shown in Fig. 2d by lines, which used to confirm the experimental results.

Realization of the CDPs and spawned WPs in synthetic space. According to the previous analysis, the eigenfrequency of a single TIM is readily controllable, and the coupling (including signs and magnitudes) between two adjacent TIMs is highly tunable. All of these are sufficient for us to construct a 1-D topological super-lattice analogous to a dimerized atomic chain, where we regard TIMs as photonic orbitals. The hybridization of them forms hybrid orbitals, which are referred to as super-modes here. As a consequence, we deliberately design an optical superlattice to create a periodic sequence of TIMs, which is built up of alternating structures of p_m, D_A, q_n, and D_B, as illustrated in Fig. 3a. The i-th unit dimer with two sublattice sites A_i and B_i is defined as $[p_{m/2}D_Aq_nD_Bp_{m/2}]$ marked by the magenta dashed rectangle in Fig. 3a. In this notation, the subscripts A and B denote two different defective units with their respective thickness d_A and d_B, and the subscripts $m(n)$ labels the number of unit cells of the q (p)-type PC. We then express the on-site resonance frequencies of two adjacent TIMs as $\omega_{A,s} = \omega_s + \Delta_s$ and $\omega_{B,s} = \omega_s - \Delta_s$, where $s = \uparrow\downarrow$ denoting two polarizations, $\omega_s \equiv (\omega_{A,s} + \omega_{B,s})/2$, and $\Delta_s \equiv (\omega_{A,s} - \omega_{B,s})/2$. Here, Δ_s refers to a staggered on-site frequency offset regarding ω_s as a reference value. As shown in Fig. 1, the values of Δ_s are determined by the difference $(d_A - d_B)$. The coupling PCs $q_n(p_m)$ directly determine the intra(inter)dimer coupling strength, denoted as $J_{1,s}(J_{2,s})$. What's more, a remarkable feature of our superlattice system is the adjustability of the coupling sign, since that m and n are simultaneously odd or even numbers leads to $J_{1,s}J_{2,s} > 0$, otherwise $J_{1,s}J_{2,s} < 0$. Taking this into account, we introduce an additional parameter g as $g \equiv \mathrm{sgn}\left(\frac{J_{2,s}}{J_{1,s}}\right)$, and utilize $J_s \equiv (-gJ_{1,s} - J_{2,s})/2g$ and $\delta_s \equiv (-gJ_{1,s} + J_{2,s})/2g$ for further discussion. As shown in Fig. 2, the values of δ_s are determined by $(m - n)$. Accordingly, the Hamiltonian for the super-modes formed by multiple TIMs can be written as an effective dimerized model.

$$H = \sum_{i,s=\uparrow,\downarrow} -(J_s + \delta_s)a_{i,s}^\dagger b_{i,s} - g(J_s - \delta_s)a_{i+1,s}^\dagger b_{i,s} + h.c.$$
$$+ (\omega_s + \Delta_s)a_{i,s}^\dagger a_{i,s} + (\omega_s - \Delta_s)b_{i,s}^\dagger b_{i,s} \tag{1}$$

Here, $a_{i,s}^\dagger(b_{i,s}^\dagger)$ and $a_{i,s}(b_{i,s})$ are the creation and annihilation operators of the TIM lying on $A_i(B_i)$ site of the chain, respectively. Since D_A and D_B have negligible effect on the coupling strength, δ_s and Δ_s can be treated as independent parameters (see details in the Supplementary Note 3). If we merely restrict ourselves to the case of zero in-plane wave vector ($k_x = 0\,\mu m^{-1}$), this Hamiltonian represents a novel 1-D Su–Schrieffer–Heeger (Rice–Mele) chain with $d_A = d_B(d_A \neq d_B)$ and hence $\Delta_s = 0(\Delta_s \neq 0)$, of which band structures and topological properties such as topological end states are analyzed detailedly in the Supplementary Note 4. Based on the fact that the degeneracy of TM and TE polarized TIMs lifts when $k_x \neq 0\,\mu m^{-1}$, ω_s is a function of k_x such that $\omega_s(k_x) = \omega_0 + \tau_s(k_x)$, where $\omega_0 \equiv \omega_s(0)$ denotes the eigenfrequency of the $k_x = 0\,\mu m^{-1}$ case and $\tau_s(k_x)$ refers to the frequency shift compared with ω_0. The Hamiltonian (Eq. 1) can thus be transformed into the Bloch momentum space, and expressed in the pseudospin up ($s = \uparrow$) (TM) and down ($s = \downarrow$) (TE) representation as

$$H = \tilde{\tau}\sigma_z \otimes \sigma_0 + \begin{pmatrix} \tilde{d}_\uparrow \cdot \sigma & 0 \\ 0 & \tilde{d}_\downarrow \cdot \sigma \end{pmatrix}. \tag{2}$$

Here, we introduce $(\tilde{d}_s)_x = -(J_s + \delta_s) - g(J_s - \delta_s)\cos\xi\Lambda$, $(\tilde{d}_s)_y = -g(J_s - \delta_s)\sin\xi\Lambda$, $(\tilde{d}_s)_z = \Delta_s$, and $\tilde{\tau} = \frac{1}{2}(\tau_\uparrow(k_x) - \tau_\downarrow(k_x))$, in which Λ is the length of the unit dimer, ξ serves as the Bloch wave vector in the z direction and σ stands for Pauli matrices. Thereby, the eigenvalue of the Hamiltonian (Eq. 2) could be figured out, denoted as $\tilde{\omega} \equiv \omega - \overline{\omega_0}$ with $\overline{\omega_0} = \omega_0 + \frac{1}{2}\left(\tau_\uparrow(k_x) + \tau_\downarrow(k_x)\right)$.

With respect to the special case at $k_x = 0\,\mu m^{-1}$, TM and TE polarized super-modes are degenerate since $\tilde{\tau} = 0$ and $\tilde{d}_\uparrow = \tilde{d}_\downarrow$. Hence we introduce the parameters $\delta \equiv \delta_\uparrow = \delta_\downarrow(k_x = 0\,\mu m^{-1})$ and $\Delta \equiv \Delta_\uparrow = \Delta_\downarrow(k_x = 0\mu m^{-1})$, together with the original Bloch wave vector ξ, to form a 3-D synthetic space (δ,ξ,Δ). The Hamiltonian then can be transformed into $H(\delta,\xi,\Delta) = (H_\uparrow; 0; 0, H_\downarrow)$, in which $H_{s=\uparrow,\downarrow} \equiv \tilde{d}_{s=\uparrow,\downarrow} \cdot \sigma$. As a result, the associated four bands cross at the degenerate point $(\delta,\xi,\Delta) = (0, 0, 0)$. To characterize this degenerate point, we expand the two-by-two Hamiltonian H_s around it:

$$H_s = \delta v_{\delta x,s}\sigma_x + \xi v_{\xi y,s}\sigma_y + \Delta v_{\Delta z,s}\sigma_z, \tag{3}$$

where $v_{\delta x,s} = -2$, $v_{\xi y,s} = \Lambda J_s$, and $v_{\Delta z,s} = 1$ (see "seehods"). The above Hamiltonian exhibits a standard Weyl Hamiltonian form, and thus the band crossing point for either TM or TE super-modes can be regarded as a WP in the synthetic space. An important characteristic of a WP is the capacity to carry a topological charge, which corresponds to its chirality $c_s(= \pm 1)$. The Hamiltonian (Eq. 3) possesses the form of $H(q) = q_i v_{ij}\sigma_j$ with $c_s = \mathrm{sgn}\left(\det\left[v_{ij,s}\right]\right)$, indicating that c_s is equal to $-\mathrm{sgn}(J_s)$. This shows that the chirality c_s of WPs relies on the sign of J_s, which is decided by the parity of $m(n)$ (See details in the Supplementary Note 5). According to the degeneracy of TM and TE polarized super-modes when $k_x = 0\,\mu m^{-1}$, $c_\uparrow = c_\downarrow$ such that the four-band Hamiltonian indicates an overlapping of two WPs with the same topological charge in synthetic space. Shown in Fig. 3b as a transparent blue cone in the $\delta - \Delta$ space at $\xi = 0$, such kind of band crossing is known as Charge-2 Dirac point (CDP), whose Hamiltonian is the direct sum of two identical spin-1/2 WPs at the Brillouin zone center and thus has a Chern number of ± 2, contrary to a conventional 3-D Dirac point consisting of two WPs with opposite Chern numbers. The band dispersion in the $(\xi,\Delta) = (0,0)$ plane (highlighted by black solid lines in Fig. 3b) is illustrated in Fig. 3c, showing linear property adjacent to the degenerate point. Through such a way, we have provided a novel
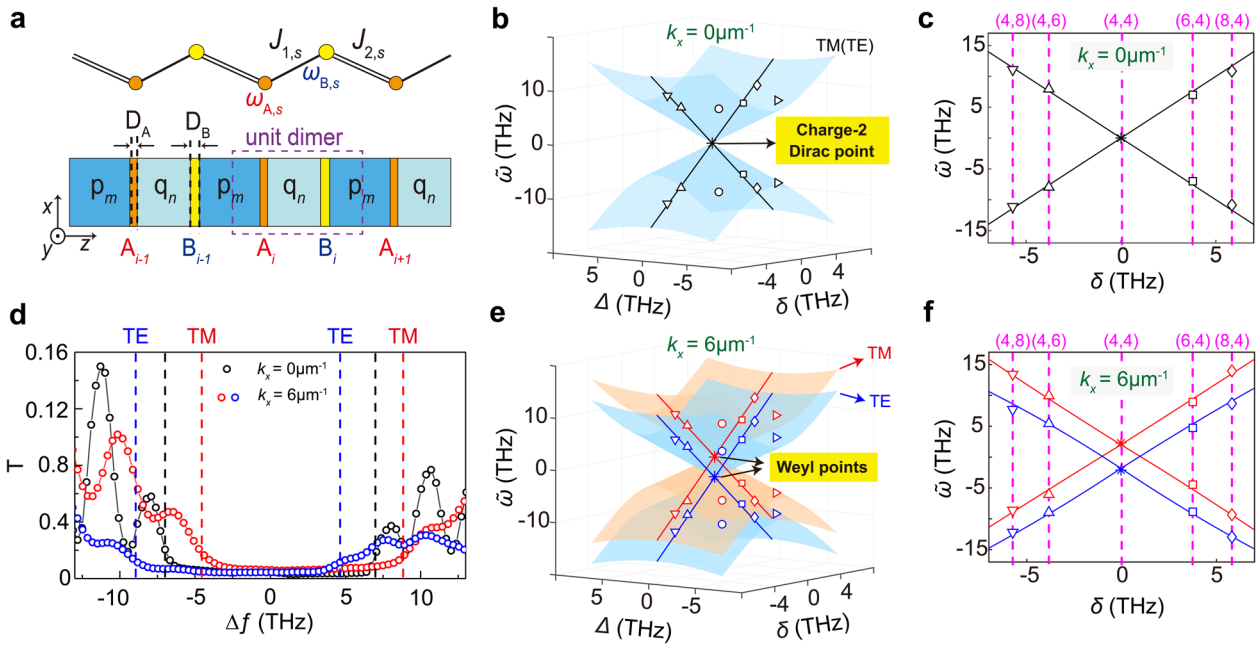
Fig. 3 Realization of a Charge-2 Dirac point and its evolvement into Weyl points in synthetic space. a The superlattice of topological interface modes (TIMs) is shown in the lower panel, and the schematic representation of effective dimerized model is given in the upper panel. **b** Measured transmission spectra as a function of Δf for the sample with $(m,n) = (6,4)$ and $(d_A, d_B) = (0,0)$ $((\delta,\xi,\Delta) = (3.8,0,0))$ under normal incidence $(k_x = 0\ \mu m^{-1})$ and oblique incidence of transverse-magnetic/transverse-electric TE/TM waves $(k_x = 6\ \mu m^{-1})$. **c, d** Eigenfrequency surface in the $\delta - \Delta$ space at **c** $k_x = 0\ \mu m^{-1}$ and (**d**) $k_x = 6\ \mu m^{-1}$. The upward-pointing triangles, downward-pointing triangles, squares, and rhombuses mark the bulk band edge frequencies obtained from experimental data of four samples with $(m,n) = (4,6), (4,8), (6,4),$ and $(8,4)$, respectively. The asterisks stand for the center of two gapless bands of super-modes by measuring transmission spectra of the sample with $(m,n) = (4,4)$. The thickness of defective units (expressed in nanometers) for all the five samples are $(d_A, d_B) = (0,0)$. The associated synthetic coordinates (δ,ξ,Δ) endowed with units of (THz, μm^{-1}, THz) for these five sample are $(0,0,0)$, $(-3.8,0,0)$, $(-5.7,0,0)$, $(3.8,0,0)$, and $(5.8,0,0)$ as labelled in **e** and **f**. The open circles and right-pointing triangles also represent experimental band edge frequencies of another two samples with $(m,n) = (4,6)$ and $(6,4)$, and the thickness of their defective units are $(d_A, d_B) = (3,0)$, corresponding to $(\delta,\xi,\Delta) = (-3.8,0,-4.1)$ and $(3.8,0,-4.1)$, respectively. Solid lines highlight the $\Delta = 0$ plane. **e, f** Eigenfrequency as a function of δ at $\xi = 0$ and $\Delta = 0$ when (**e**) $k_x = 0\ \mu m^{-1}$ and **f** $k_x = 6\ \mu m^{-1}$. Solid lines are calculated by the effective dimerized model, and open markers are experimental results with their samples labelled on the top.

method to realize the generalized CDPs with $c = \sum_s c_s = \pm 2$ in the optical frequency regime by manipulations of 1-D optical superlattices exploring the concept of synthetic dimensions.

Such a four-fold cone can be detected unambiguously in experiment. We start by making five samples with structural parameters $(m,n) = (4,4), (4,6), (4,8), (6,4),$ and $(8,4)$, respectively, featured by $d_A = d_B$ such that $\Delta = 0$. We then measure the transmission spectra under normal incidence for these five samples to obtain locations of $\tilde{\omega}$. Figure 3d presents the transmission spectra as a function of Δf (utilizing $\overline{\omega_0}$ as the reference) for the sample $(m,n) = (6,4)$, where the black dashed lines emphasize the super-modes band edges. In Fig. 3b, c, we employ black squares to mark locations of such band edges, which almost lie on the crossing lines indicating a great agreement with the theory. The locations of $\tilde{\omega}$ for other four samples are plotted as well by different dots in Fig. 3b, c, all of which are situated at the crossing lines and thus exhibit the characteristic of linear crossing for the Dirac point, matching with the theory quite well (See details in the Supplementary Note 6). Moreover, we fabricate another two samples with $(m,n) = (4,6)$ and $(6,4)$, characterized by $d_A \neq d_B$ and hence $\Delta \neq 0$. The results gotten from experimental data are also shown in Fig. 3b, well-located at the cone's surface. Consequently, the experimental results support our theory of the CDP, and hence the realization of a CDP in the visible light range is achieved.

When $k_x \neq 0\ \mu m^{-1}$, the degeneracy of TM and TE super-modes is removed, lending to $\tilde{\tau} \neq 0$ and $\tilde{d}_\uparrow \neq \tilde{d}_\downarrow$. Therefore, nonzero k_x

will split the CDP at $k_x = 0\ \mu m^{-1}$ into two WPs of TM and TE polarized super-modes, respectively. The solid surface in Fig. 3e shows such two WPs in the $\delta - \Delta$ space at $\xi = 0$ with $k_x = 6\ \mu m^{-1}$, and the dispersion in the $(\xi,\Delta) = (0,0)$ plane are present in Fig. 3f by red(blue) solid lines for TM(TE) modes. To demonstrate it, we measure the transmission spectra under oblique incident light of the seven samples defined in Fig. 3b, c. We choose to show the transmission spectra of the sample $(m,n) = (6,4)$ in Fig. 3d, and the band edges of the super-modes for TM and TE polarizations are highlighted by red and blue vertical lines. We see that the band edges red-shifted (blue-shifted) for TE (TM) polarization, which agrees with theoretical results in Fig. 3e. We further mark the locations of associated $\tilde{\omega}$ of all these samples in Fig. 3e, f with red (blue) color for the TM (TE) super-modes. The consistency between the theory and experiments indubitably corroborates our idea that the CDP is separated into two WPs in the synthetic space with the frequency splitting equals $2\tilde{\tau}$ resulting from the nonzero k_x. As a result, $\tilde{\tau}$ can be treated as the effective Zeeman term, which increases with the enhancement of the "magnetic field" (that is, the increase of k_x). Note that varying k_x has no effect on c_s of both WPs, so $c_\uparrow = c_\downarrow$ as those of $k_x = 0\ \mu m^{-1}$ (See details in the Supplementary Note 5).

Topological end modes in truncated optical superlattices. In contrast to the conventional 3-D DPs, which carry no net topological charge and thus are lack of topological surface states, the CDPs arising in our system characterized by Chern numbers
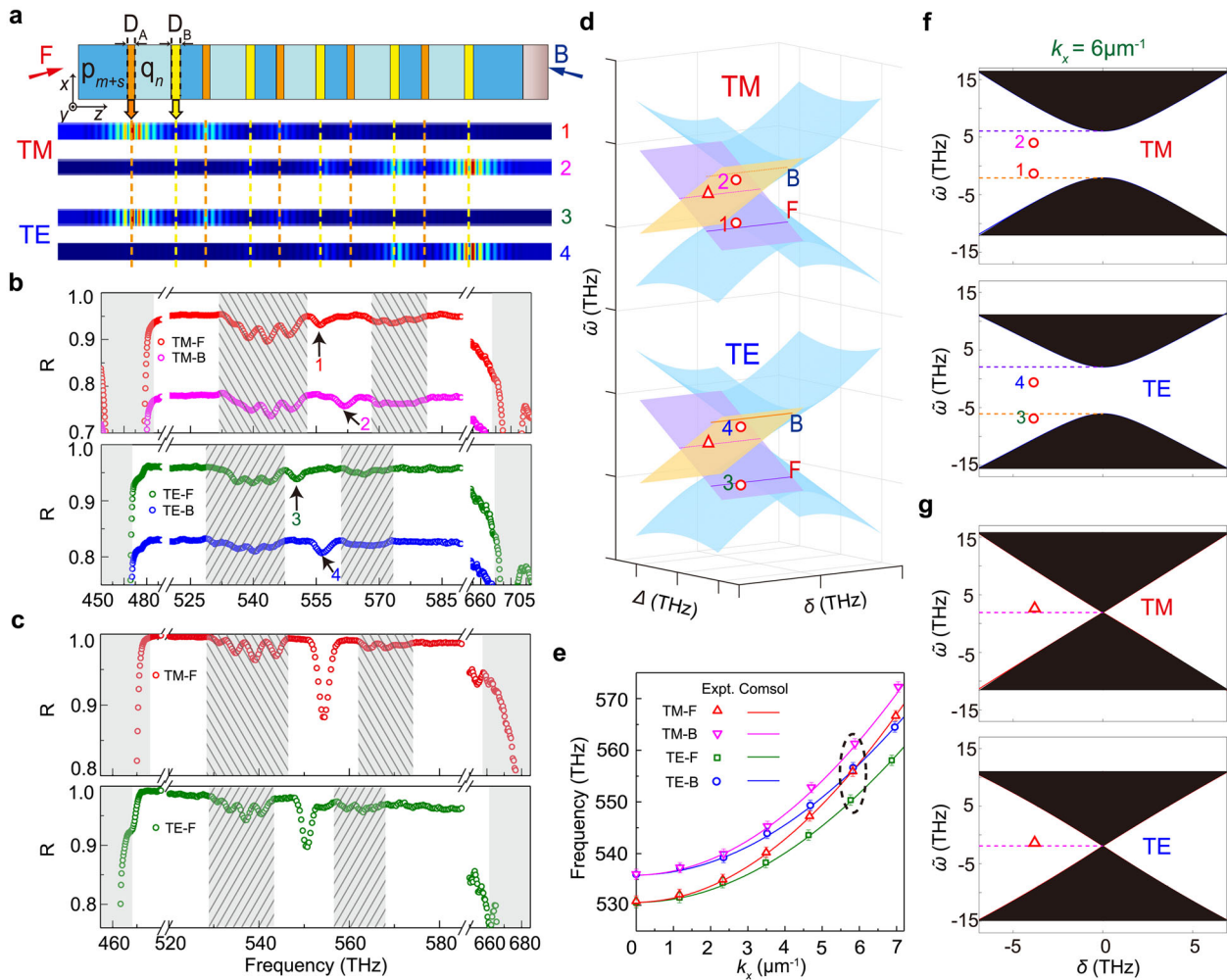
Fig. 4 Topological end states in truncated optical superlattices. a The upper panel: the schematic picture of the truncated optical superlattice $p_5[p_2D_Aq_6D_Bp_2]_5p_5$ with $(d_A,d_B) = (3,0)$ and $(\delta,\xi,\Delta) = (-3.8,0,-4.1)$. The lower panel: distributions of the electric field norm of topological end modes 1–4. **b** Measured reflection spectra of the sample depicted in **a** for transverse-magnetic (TM) and transverse-electric (TE) polarizations excited by both F and B oblique incident light with an angle of 30°. The four dips marked with black arrows correspond to topological end states 1–4. **c** Measured reflection spectra of the sample $p_5[p_2D_Aq_6D_Bp_2]_5p_5$ with $(d_A,d_B) = (0,0)$ $((\delta,\xi,\Delta) = (-3.8,0,0))$ for TM and TE polarizations excited by F incident light with an angle of 30°. **d** Eigenfrequency surfaces showing two WPs (transparent blue cones) and topological ends modes (purple and orange sheets) in the $\delta - \Delta$ space with $k_x = 6\,\mu m^{-1}$ for both TM and TE polarizations. The experimental dips in **b** and **c** are labelled by open circles and upward-pointing triangles, respectively. For display purpose, the vertical distance between two Weyl points is deliberately magnified. **e** Frequencies of topological end modes for TM and TE polarizations as a function of k_x for the sample used in **a** and **b**. The solid lines are results of numerical calculations, the open markers are obtained directly from experimental data, and experimental uncertainties are shown by error bars. The topological end states 1–4 shown in **b** are encircled by a black dashed ellipse. **f**, **g** Eigenfrequencies of topological end states for TM and TE polarizations in the **f** $\Delta = -4.1\,THz$ and **g** $\Delta = 0\,THz$ plane. The black regions in **f** and **g** refer to the bands of super-modes and the dashed lines in **d**, **f**, and **g** correspond to the calculated dispersion of topological end modes.

equal to ±2 imply the existence of intriguing topological end modes. Such end modes originate from each of the two WPs guaranteed by the bulk-edge correspondence, known as one of the most significant experimental properties of WPs. In our synthetic space, these topologically protected modes can be separated into two groups due to TM and TE polarized super-modes, respectively, each of which is supposed to be engineered independently under different polarizations. In what follows we demonstrate their existence in our optical superlattice system when truncated in space. The configurations could be generalized as $p_s[p_{m/2}D_Aq_nD_Bp_{m/2}]_5p_s$, which are composed of 5 unit dimes with an open condition along z-axis and are extended by s additional unit cells of at both termini to avoid interacting with external environment. Figure 4a sketches a specific structure with $(m,n,s) = (4,6,5)$ and $d_A \neq d_B$ such that $\delta < 0$ and $\Delta \neq 0$, meeting

the condition of supporting two nondegenerate end states (See "Methods"). The substrate is made from SiO_2 at the bottom of the structure. We describe the incident light from the front (bottom) as F (B). Topological end modes should come in pairs regardless of the value of Δ, but it is Δ that determines locations of these two end states in synthetic space, as experimentally demonstrated in Fig. 4b, c. To make it clear, in Fig. 4d we depict eigenfrequency surfaces of WPs and corresponding topological ends modes in the $\delta - \Delta$ space with $k_x = 6\,\mu m^{-1}$ for both TM and TE polarized super-modes. In Fig. 4d, the end modes on purple sheets are located at the front side of truncated chains with $\tilde{\omega} = \pm\tilde{\tau} + \Delta$ and can only be excited by F, whereas those on orange sheets are localized at the end of the chains with $\tilde{\omega} = \pm\tilde{\tau} - \Delta$ excited only by B, in which the first plus (minus) sign applies to TM (TE) polarized end modes. Notably, the end states

belonging to the intersections of the two sheets connect to the WPs, sharing the same mathematical origin as that of the Fermi-arc surface states[1,3,6] in Weyl semimetals. They are plotted by magenta dotted lines, with $\Delta = 0$ and $\tilde{\omega} = \pm \tilde{\tau}$ in synthetic space, and hence they can be excited by either F or B. It is, however, indispensable to underscore here that the Fermi-arc links two WPs in a periodically arranged system while the Fermi-arc-like end modes in our system connect a WP to the boundary of synthetic space explained by the existence of the net topological charge.

Figure 4b presents the measured reflection spectra of the sample illustrated in Fig. 4a for TM and TE polarizations excited by both F and B with an oblique incident angle of 30°, where we observe four dips inside the TIM gaps. These modes are labelled as 1–4, whose distributions of the electric field norm are exhibited in Fig. 4a. It is worth noting that, for both TM and TE polarized super-modes, the modes excited by F (1 and 3) and B (2 and 4) are located at the front and bottom of the sample, respectively. We then investigate another sample with $(m,n,s) = (4,6,5)$ and $d_A = d_B$, characterized by $\delta < 0$ and $\Delta = 0$. Its measured reflection spectra achieved from F with an incident angle of 30° for TM and TE polarizations are exhibited in Fig. 4c, where each dip in the gap of super-modes is attributed to two degenerate end modes localized at both termini. In Fig. 4b, c, transparent gray regions correspond to the common bulk band gaps of PC-p and PC-q, and the gray regions with extra inclined downward and upward lines stands for the bands of TM and TE polarized super-modes, respectively. Due to the fact that the introduction of the nonzero k_x leads to a removal of the degeneracy between TM and TE polarized end modes, each mode divides into two states with the splitting increasing rapidly as k_x increases, as revealed in Fig. 4e for the sample described in Fig. 4a. In addition, Fig. 4f, g provide projected dispersion cones within different Δ planes. The eigenfrequency surfaces of topological end modes are projected as straight dashed line and the locations of end modes mentioned above are plotted in corresponding planes. Therefore, the great conformance between calculations and experiments further verifies our argument of topological end modes based on the established optical superlattice system.

Discussion

As a burgeoning field of topological physics, the study of topological photonics has captured huge attention in recent years[49]. A wide range of photonic systems have been devoted to this field, such as waveguide arrays[50,51], coupled silicon ring resonators[52], and polariton superstructures[53], achieving remarkable accomplishments in various branches. In particular, the importance of 3-D gapless states such as Weyl and multi-Weyl points is a strong driver of current research in topological photonics. The concept of synthetic dimensions, though initially introduced to explore the higher dimensional physics by parametric coupling between internal modes or by dynamically scanning over the parameter space, has been extended and developing rapidly in the realm of Weyl or Weyl-related physics[26,27,30,34,36,37]. Relevant photonic systems include photonic crystals[26], 1-D circuit-QED lattices[36], and 2-D ring resonator lattices[37]. The essential phenomena owing to these gapless phases such as bulk-edge correspondence should be viewed in synthetic space accordingly, but still can reflect the topological characters (e.g., Chern number) of these points, just like what we have done with synthetic dimensions in this work.

Thanks to the availability and adjustability of our 1-D superlattice system, we can investigate fundamental topological features of the CDP—a novel kind of multi-Weyl points—in the photonic context by the aid of synthetic dimensions. We demonstrate the highly tunable on-site resonance frequency of

each TIM and the controlled periodic coupling of nearest-neighbor TIMs within our superlattices. The TIMs play the role of photonic orbitals, and their hybridizations form topological super-modes, whose band structures can be ingeniously engineered to create CDPs in synthetic space with the pseudospin degree originating from the polarized property of light. It is, for the first time, to realize CDPs in the visible region. Without the help of synthetic dimensions, as well as the utilization of pseudospins which fundamentally change the system's behaviors, the creation of CDPs is more demanding, possible only in the infrared range restrained by obstacles to the fabrication of complex structures. Furthermore, the CDP can be artificially split into two spawned WPs with the same Chern number by introducing nonzero horizontal wave vector that removes the degeneracy between TM and TE polarized super-modes. Such amazing process has not been obtained in previous studies, thus opening a new frontier to explore emergent phenomena of topological physics. In addition, the approach of experimental detection we render here is facile and obtainable by measuring transmission and reflection spectra to examine band structures of super-modes unambiguously. It is noteworthy that the bulk-edge correspondence displays itself as topological end modes exclusive to the CDP, residing at boundaries of truncated superlattices, which can be manipulated with ease and hence be applied for local field enhancement in various realms[45–47].

Although our system was engineered to explore CDPs in the optical region at first, it offers a versatile approach to investigating other prevailing topological physics. Notably, the CDPs in our system are, in essence, a sort of secondary topological phases. It arises due to the fact that each TIM itself is of topological origin, and hence the CDPs could be treated as a consequence of coupling among multiple TIMs. Nowadays, the secondary topological effects arouse great interest and curiosity, and various systems have been devoted to this novel field[54–56]. Our work thus presents the core concepts similar to these systems, and exhibits intriguing secondary topological signatures, as shown in Fig. 4 where topological end states lying in the tight-binding gaps of TIMs. Another hot topic on topological photonics is the exploration of non-Hermitian effects[51,57–64], which highlights itself as the appearance of exceptional points[57,59], rings[51], and surfaces[64]. By harnessing absorptive losses, our system has the potential to control imaginary parts of the TIMs' eigenfrequencies (See details in Supplementary Note 7), and then can be exploited to realize exceptional points and associated non-Hermitian effects. In addition, we may research on nonlinear topological phenomena by utilizing materials with intensity-dependent refractive indexes, which are currently a hotspot and can hold great promise for applications[65,66].

Methods

Tight-binding analysis of coupling effects. In this section we provide the approach we used to obtain normalized coupling strength between nearest-neighbor TIMs. Since the TIMs are highly localized modes that decay rapidly into bulks, we can apply the tight-binding method to analyze such coupling effects. For the cases illustrated in Fig. 2a, the Hamiltonian can be written as the following matrix:

$$H = \begin{pmatrix} \omega_0 & t \\ t & \omega_0 \end{pmatrix} \qquad (4)$$

where ω_0 is the eigenvalue of either TIM and t corresponds to the coupling term.

Diagonalizing the Hamiltonian matrix (Eq. 4), we achieved two eigenstates with eigenfrequencies and wave functions given by:

$$\omega = \begin{cases} \omega_s \equiv \omega_0 + t, & |\varphi^S\rangle = \frac{\sqrt{2}}{2}(|\phi_1\rangle + |\phi_2\rangle) \\ \omega_{AS} \equiv \omega_0 - t, & |\varphi^{AS}\rangle = \frac{\sqrt{2}}{2}(|\phi_1\rangle - |\phi_2\rangle) \end{cases} \qquad (5)$$

Here, $|\phi_1\rangle$ and $|\phi_2\rangle$ are the wave functions of the TIMs trapped by two identical defective units. $|\varphi^S\rangle$ and $|\varphi^{AS}\rangle$ are the emergent symmetric (S) and antisymmetric

(AS) coupling modes as described in the text. As a result, the normalized coupling strength can be written by definition as:

$$J \equiv \frac{t}{\omega_0} = \frac{\omega_S - \omega_{AS}}{2\omega_0}. \tag{6}$$

To calculate the value of J as a function of N for both p-type and q-type PCs, as well as the in-plane wave vector k_x for both TM and TE polarizations, a series of numerical simulations were performed by means of COMSOL Multiphysics via the optic module. The results are shown in Fig. 2c, d, and the distributions of electric field profiles for some specific configurations are exhibited in Supplementary Fig. 1.

In the experimental measurements, we harnessed the transmission spectra of each sample under normal or oblique incidence, where two transmission peaks attribute to two coupling TIMs (S and AS), and hence found the value of J. The outcomes are present in Fig. 2, matching well with the tight-binding analysis. During this procedure we treated k_x as a constant with certain incident angle, since the range of working frequency is so small that k_x is little influenced by the frequency variation. Strictly speaking, this treatment could be another reason (additional to the fabrication imperfection and experimental errors) that the measurements are slightly deviated from the simulations on frequencies, but it has minimal impact on the value of J. Therefore, error bars used in Fig. 2c, d only result from the broadening transmission peaks owing to experimental uncertainties.

Deduction of the Hamiltonian for the CDP. The Hamiltonian (Eq. 2) can be expressed as $H(\delta, \xi, \Delta) = (H_\uparrow; 0, H_\downarrow)$ with $H_{s=\uparrow,\downarrow} \equiv \tilde{d}_{s=\uparrow,\downarrow} \cdot \sigma$ when $k_x = 0 \, \mu m^{-1}$. We argued that H_s for super-modes with respective TM and TE polarizations exhibit the same standard Weyl Hamiltonian form near the degenerate point $(\delta, \xi, \Delta) = (0,0,0)$. Here, we elaborate on the deductive process of such Weyl Hamiltonian, and hence acquire the Hamiltonian for the CDP. Since $\left(\tilde{d}_s\right)_x = -(J_s + \delta_s) - g(J_s - \delta_s)\cos \xi\Lambda$, $\left(\tilde{d}_s\right)_y = -g(J_s - \delta_s)\sin \xi\Lambda$, and $\left(\tilde{d}_s\right)_z = \Delta_s$ within H_s, in which $\delta \equiv \delta_\uparrow = \delta_\downarrow$ and $\Delta \equiv \Delta_\uparrow = \Delta_\downarrow$ given $k_x = 0 \mu m^{-1}$. Note that $\delta = 0$ indicates $m = n$ in the unit dimer, resulting in $g = -1$. Thereby, keeping only the terms at the lowest order of δ, ξ, and Δ around the degenerate point $(0,0,0)$, $\left(\tilde{d}_s\right)_x = -(J_s + \delta) + (J_s - \delta) = -2\delta$, $\left(\tilde{d}_s\right)_y = (J_s - \delta) \cdot \xi\Lambda = -\Lambda J_s\xi$ and $\left(\tilde{d}_s\right)_z = \Delta$, and thus H_s can be written in the basis of Pauli matrices as:

$$H_s = -2\delta\sigma_x + \Lambda J_s\xi\sigma_y + \Delta\sigma_z \tag{7}$$

which exactly corresponds to a WP in synthetic space. Furthermore, the TM and TE polarized super-modes are degenerate when $k_x = 0 \, \mu m^{-1}$, so that the four-band Hamiltonian (Eq. 2) near the degenerate point $(\delta, \xi, \Delta) = (0,0,0)$ reveals an overlapping of two identical WPs, namely, the CDP.

Eigenfrequency surfaces of topological end modes. The bulk-edge correspondence of spawned WPs formed in our synthetic space is guaranteed by the topologically nontrivial property of the truncated superlattice. This kind of superlattice must meet the condition that the absolute value of the coupling strength within a unit dimer is less than that between two adjacent dimers, no matter what value Δ takes. Consequently, if both m and n are even numbers such that $J_s < 0$, δ must be negative and the corresponding eigenfrequency surfaces of topological end modes are plotted in Fig. 4d. However, if m and n are simultaneously odd, $J_s > 0$ and δ must be positive, making the eigenfrequency surfaces of topological end modes become the reflection of those shown in Fig. 4d in the plane $\delta = 0$.

Data availability

The data that support the findings of this study are available from the corresponding author on reasonable request.

References

1. Wan, X., Turner, A. M., Vishwanath, A. & Savrasov, S. Y. Topological semimetal and Fermi-arc surface states in the electronic structure of Syrochlore Iridates. *Phys. Rev. B.* **83**, 205101 (2011).
2. Lv, B. Q. et al. Experimental discovery of Weyl semimetal TaAs. *Phys. Rev. X.* **5**, 031013 (2015).
3. Xu, S.-Y. et al. Discovery of a Weyl Fermion semimetal and topological Fermi arcs. *Science* **349**, 613 (2015).
4. Lu, L. et al. Experimental observation of Weyl points. *Science* **349**, 622 (2015).
5. Soluyanov, A. A. et al. Type-II Weyl semimetals. *Nature* **527**, 495 (2015).
6. Deng, K. et al. Experimental observation of topological Fermi arcs in Type-II Weyl semimetal MoTe₂. *Nat. Phys.* **12**, 1105 (2016).
7. Liu, Z. K. et al. Discovery of a three-dimensional topological Dirac semimetal, Na₃Bi. *Science* **343**, 864 (2014).
8. Armitage, N., Mele, E. & Vishwanath, A. Weyl and Dirac semimetals in three-dimensional solids. *Rev. Mod. Phys.* **90**, 015001 (2018).
9. Xu, S.-Y. et al. Discovery of a Weyl Fermion state with Fermi arcs in Niobium Arsenide. *Nat. Phys.* **11**, 748 (2015).
10. Fang, C., Gilbert, M. J., Dai, X. & Bernevig, B. A. Multi-Weyl topological semimetals stabilized by point group symmetry. *Phys. Rev. Lett.* **108**, 266802 (2012).
11. Bradlyn, B. et al. Beyond Dirac and Weyl Fermions: unconventional quasiparticles in conventional crystals. *Science* **353**, aaf5037 (2016).
12. Tang, P., Zhou, Q. & Zhang, S.–C. Multiple types of topological Fermions in transition metal Silicides. *Phys. Rev. Lett.* **119**, 206402 (2017).
13. Lv, B. Q. et al. Observation of three-component Fermions in the topological semimetal Molybdenum Phosphide. *Nature* **546**, 627 (2017).
14. Zhang, T. et al. Double-Weyl phonons in transition-metal Monosilicides. *Phys. Rev. Lett.* **120**, 016401 (2018).
15. Miao, H. et al. Observation of double Weyl phonons in parity-breaking FeSi. *Phys. Rev. Lett.* **121**, 035302 (2018).
16. Sanchez, D. S. et al. Topological chiral crystals with helicoid-arc quantum states. *Nature* **567**, 500 (2019).
17. Schröter, N. et al. Chiral Topological semimetal with multifold band crossings and long Fermi arcs. *Nat. Phys.* **15**, 759 (2019).
18. Rao, Z.-C. et al. Observation of unconventional chiral Fermions with long Fermi arcs in CoSi. *Nature* **567**, 496 (2019).
19. Dubček, T. et al. Weyl points in three-dimensional optical lattices: synthetic magnetic monopoles in momentum space. *Phys. Rev. Lett.* **114**, 225301 (2015).
20. Xu, Y., Zhang, F. & Zhang, C. Structured Weyl points in spin-orbit coupled Fermionic superfluids. *Phys. Rev. Lett.* **115**, 265304 (2015).
21. Xiao, M., Lin, Q. & Fan, S. Hyperbolic Weyl point in reciprocal chiral metamaterials. *Phys. Rev. Lett.* **117**, 057401 (2016).
22. Chen, W.-J., Xiao, M. & Chan, C. T. Photonic crystals possessing multiple Weyl points and the experimental observation of robust surface states. *Nat. Commun.* **7**, 13038 (2016).
23. Noh, J. et al. Experimental observation of optical Weyl points and Fermi arc-like surface states. *Nat. Phys.* **13**, 611 (2017).
24. Yang, B. et al. Ideal Weyl points and helicoid surface states in artificial photonic crystal structures. *Science* **359**, 1013 (2018).
25. Saba, M., Hamm, J. M., Baumberg, J. J. & Hess, O. Group theoretical route to deterministic Weyl points in chiral photonic lattices. *Phys. Rev. Lett.* **119**, 227401 (2017).
26. Wang, Q., Xiao, M., Liu, H., Zhu, S. & Chan, C. T. Optical interface states protected by synthetic Weyl points. *Phys. Rev. X.* **7**, 031032 (2017).
27. Xiao, M., Chen, W.-J., He, W.-Y. & Chan, C. T. Synthetic gauge flux and Weyl points in acoustic systems. *Nat. Phys.* **11**, 920 (2015).
28. Yang, Z. & Zhang, B. Acoustic Type-II Weyl nodes from stacking dimerized chains. *Phys. Rev. Lett.* **117**, 224301 (2016).
29. He, H. et al. Topological negative refraction of surface acoustic waves in a Weyl phononic crystal. *Nature* **560**, 61 (2018).
30. Fan, X. et al. Probing Weyl physics with one-dimensional sonic crystals. *Phys. Rev. Lett.* **122**, 136802 (2019).
31. Roushan, P. et al. Observation of topological transitions in interacting quantum circuits. *Nature* **515**, 241 (2014).
32. Schroer, M. D. et al. Measuring a topological transition in an artificial spin-1/2 system. *Phys. Rev. Lett.* **113**, 050402 (2014).
33. Riwar, R.-P., Houzet, M., Meyer, J. S. & Nazarov, Y. V. Multi-terminal Josephson junctions as topological matter. *Nat. Commun.* **7**, 11167 (2016).
34. Yuan, L., Lin, Q., Xiao, M. & Fan, S. Synthetic dimension in photonics. *Optica* **5**, 1396 (2018).
35. Dutt, A. et al. A single photonic cavity with two independent physical synthetic dimensions. *Science* **367**, 59–64 (2020).
36. Mei, F. et al. Witnessing topological Weyl semimetal phase in a minimal circuit-QED lattice. *Quantum Sci. Technol.* **1**, 015006 (2016).
37. Lin, Q. et al. Photonic Weyl point in a two dimensional resonator lattice with a synthetic frequency dimension. *Nat. Commun.* **7**, 13731 (2016).
38. Yang, Y. et al. Topological triply degenerate point with double Fermi arcs. *Nat. Phys.* **15**, 645 (2019).
39. Bradlyn, B. et al. Topological quantum chemistry. *Nature* **547**, 298 (2017).
40. Mourik, V. et al. Signatures of Majorana Fermions in hybrid superconductor-semiconductor nanowire devices. *Science* **336**, 1003 (2012).
41. Gröning, O. et al. Engineering of robust topological quantum phases in Graphene nanoribbons. *Nature* **560**, 209 (2018).
42. Rizzo, D. J. et al. Topological band engineering of Graphene nanoribbons. *Nature* **560**, 204 (2018).
43. Belopolski, I. et al. A novel artificial condensed matter lattice and a new platform for one-dimensional topological phases. *Sci. Adv.* **3**, e1501692 (2017).
44. Rudner, M. S., Lindner, N. H., Berg, E. & Levin, M. Anomalous edge states and the bulk-edge correspondence for periodically driven two-dimensional systems. *Phys. Rev. X.* **3**, 031005 (2013).
45. Lheureux, G. et al. Polarization-controlled confined Tamm plasmon lasers. *ACS Photonics* **2**, 842 (2015).

46. Gazzano, O. et al. Single photon source using confined Tamm plasmon modes. *Appl. Phys. Lett.* **100**, 232111 (2012).
47. Chen, Y. K. et al. Back focal plane imaging of Tamm plasmons and their coupled emission. *Laser Photonics Rev.* **8**, 933 (2014).
48. Choi, K. H., Ling, C. W., Lee, K. F., Tsang, Y. H. & Fung, K. H. Simultaneous multi-frequency topological edge modes between one-dimensional photonic crystals. *Opt. Lett.* **41**, 1644 (2016).
49. Ozawa, T. et al. Topological photonics. *Rev. Mod. Phys.* **91**, 015006 (2019).
50. Kraus, Y. E., Lahini, Y., Ringel, Z., Verbin, M. & Zilberberg, O. Topological states and adiabatic pumping in quasicrystals. *Phys. Rev. Lett.* **109**, 106402 (2012).
51. Cerjan, A. et al. Experimental realization of a Weyl exceptional ring. *Nat. Photonics* **13**, 623–628 (2019).
52. Mittal, S. et al. Measurement of topological invariants in a 2D photonic system. *Nat. Photonics* **10**, 180–183 (2016).
53. Baboux, F. et al. Measuring topological invariants from generalized edge states in polaritonic quasicrystals. *Phys. Rev. B.* **95**, 161114(R) (2017).
54. Serra-Garcia, M. et al. Observation of a phononic quadrupole topological insulator. *Nature* **555**, 342 (2018).
55. Mittal, S. et al. Photonic quadrupole topological phases. *Nat. Photonics* **13**, 692–696 (2019).
56. Xue, H. et al. Acoustic higher-order topological insulator on a kagome lattice. *Nat. Mater.* **18**, 108–112 (2019).
57. Feng, L., Wong, Z. J., Ma, R.-M., Wang, Y. & Zhang, X. Single-mode laser by parity-time symmetry breaking. *Science* **346**, 972–975 (2014).
58. Zeuner, J. M. et al. Observation of a topological transition in the bulk of a non-Hermitian system. *Phys. Rev. Lett.* **115**, 040402 (2015).
59. Ding, K., Ma, G., Xiao, M., Zhang, Z. & Chan, C. T. Emergence, coalescence, and topological properties of multiple exceptional points and their experimental realization. *Phys. Rev. X.* **6**, 021007 (2016).
60. Leykam, D., Bliokh, K. Y., Huang, C., Chong, Y. & Nori, F. Edge modes, degeneracies, and topological numbers in non-Hermitian systems. *Phys. Rev. Lett.* **118**, 040401 (2017).
61. Shen, H., Zhen, B. & Fu, L. Topological band theory for non-Hermitian Hamiltonians. *Phys. Rev. Lett.* **120**, 146402 (2018).
62. Gong, Z. et al. Topological phases of non-Hermitian systems. *Phys. Rev. X.* **8**, 031079 (2018).
63. Kremer, M. et al. Demonstration of a two-dimensional PT-symmetric crystal. *Nat. Commun.* **10**, 435 (2019).
64. Zhang, X., Ding, K., Zhou, X., Xu, J. & Jin, D. Experimental observation of an exceptional surface in synthetic dimensions with magnon polaritons. *Phys. Rev. Lett.* **123**, 237202 (2019).
65. Hadad, Y., Khanikaev, A. B. & Alù, A. Self-induced topological transitions and edge states supported by nonlinear staggered potentials. *Phys. Rev. B.* **93**, 155112 (2016).
66. Leykam, D. & Chong, Y. Edge solitons in nonlinear photonic topological insulators. *Phys. Rev. Lett.* **117**, 143901 (2016).

Author contributions

M.H. proposed and designed the system. M.H., T.Q., and X.J. carried out the experiments. M.H., K.D., Q.W., H.L., and S.Z. contributed to the experimental characterization and interpretation and developed the theory. M.H. and K.D. co-wrote the manuscript. All of the authors were involved in the discussions.

Competing interests

The authors declare no competing interests.

Additional information

Supplementary information is available for this paper at https://doi.org/10.1038/s42005-020-00395-1.

Correspondence and requests for materials should be addressed to H.L.

Reprints and permission information is available at http://www.nature.com/reprints

Publisher's note Springer Nature remains neutral with regard to jurisdictional claims in published maps and institutional affiliations.